 CMES, vol.13, no.3, pp.199-217, 2006

Thermomechanical Analysis of Functionally Graded Composites under Laser Heating by the MLPG Method

H. K. Ching[1,2] **and J. K. Chen**[2]

Abstract: The Meshless Local Petrov-Galerkin (MLPG) method is a novel numerical approach similar to finite element methods, but it allows the construction of the shape function and domain discretization without defining elements. In this study, the MLPG analysis for transient thermomechanical response of a functionally graded composite heated by Gaussian laser beams is presented. The composite is modeled as a 2-D strip which consists of metal and ceramic phases with the volume fraction varying over the thickness. Two sets of the micromechanical models are employed for evaluating the effective material properties, respectively. Numerical results are presented for the thermomechanical responses in both the transient and steady states. A parametric study with respect to the spatial distribution and volume fraction of material constituents, the rising rate of the laser power, and the radius of the laser beam is conducted.

keyword: Meshless Particle Method, Functionally Graded Materials, MLPG, Thermomechanics, Laser Heating.

1 Introduction

In many engineering applications, ceramics are widely used as thermal barrier coating (TBC) in high temperature transient environments. While a ceramic coating provides corrosion, wear and erosion resistance, possesses higher compressive strength, and can protect the structural components from the severe thermal environment, joining the ceramic to a different material (e.g. metal substrate) can inevitably result in a large stress across the interface, thus often causing the delamination mode of failure in the coated structures. In this regard, one way to overcome this adverse effect is to use functionally graded materials (FGMs).

FGMs are advanced composite materials which are composed of two or more constituents. Typically, these materials are made from a mixture of ceramic(s) and metal(s). FGMs are microscopically heterogeneous, but the volume fractions of material constituents can be engineered to a continuously spatial variation, and in turn possess smoothly varying material properties. This allows FGMs to be optimized by grading the volume fractions of the material constituents for the desirable properties, and thus they can offer various advantages such as reduction of thermal stresses, minimization of stress concentration or intensity factors, and attenuation of stress waves. Therefore, FGMs have attracted considerable attention in the field of structural ceramic applications, which include gas turbines, heat-engine components, packaging encapsulants, thermoelectric generators, and human implants, just to name a few.

In the transient thermomechanical analysis of linearly elastic FGMs, numerous approaches have been proposed, either by the analytical form or by the numerical techniques. Noda (1999) solved the governing equations for thermal stresses in FGMs using a perturbation method, and delineated the crack propagation paths due to thermal shock. He also provided a literature review about the thermoelastic response of FGMs. Ueda (2001) utilized the micromechanical model to study the transient behavior of an FG divertor plate. By assuming an exponentially spatial variation of the material properties, Ootao and Tanigawa (2004,2005) analyzed transient thermal transport and deformation for 2-D and 3-D FG plates subjected to nonuniformly convective heat supply. Jin and Paulino (2001) solved for transient thermal stresses in an FG strip by using a multi-layered material model. Vel and Batra (2003) derived a 3-D exact solution of transient thermal stresses in an FG plate under time-dependent thermal loads on its top and/or bottom surfaces. Awaji and Sivakumar (2001) employed both the variable transformation and multi-layered techniques to study the tran-

[1] Correspondence to: J. K. Chen. Email: chenjnk@missouri.edu; fax: (573) 884-5090

[2] Department of Mechanical and Aerospace Engineering University of Missouri, Columbia MO 65201

sient deformation in an FG cylinder. Praveen, Chin and Reddy (1999) performed a finite element analysis for an FG ceramic-metal cylinder with temperature-dependent material properties and delineated the thermoelastic deformation under rapid heating. Wang and Mai (2005) and Wang and Tian (2005) presented explicit finite element formulations for analyzing FG solids.

Although analytical approaches provide closed-form solutions, they are limited to simple geometries, certain types of gradation of material properties (e.g. exponential or power law distribution), specific types of boundary conditions (e.g. simply support) and special loadings (e.g. sinusoidal loading). The above constraints can be relaxed when numerical approaches are employed, for example, finite element methods (FEMs). However, a nonhomogeneous FGM needs to be treated as numerous homogeneous elements, and thereby requiring intensive labor to generate the mesh and assign the material properties to elements. To deal with the complexity and nonhomogeneity of the properties in FGMs, a meshless method may be more suited and provides a promising cost-effective CAE tool for the design of FGM structures.

Since the last decade, the meshless particle methods have emerged as an effective numerical approach for solving initial-boundary-value problems. The feature of these methods is that only a set of scattered nodes that need not be connected to form closed polygons is required for modeling the physical domain. In contrast to the FEM, the meshless methods can save the pre-processing work of mesh generation, as no element is required in the entire model. Besides, the computed stresses and strains are smooth so that there is no need for any post-process smoothing technique. More importantly, the spatial variation of material properties in FGMs can easily be described at the level of the integration points. In the past years, a variety of meshless methods have been proposed, such as the Diffuse Element Method (DEM) (Nayroles, Touzot and Villon, 1992), the Element-Free Galerkin (EFG) method (Belytschko, Lu and Gu, 1994), the Hp-Clouds (Duarte and Oden, 1996), the Reproducing Kernel Particle Method (RKPM) (Liu, Jun and Zhang, 1995), the Partition of Unity Finite Element Method (PUFEM) (Melenk and Babuska, 1996), the Meshless Local Petrov-Galerkin (MLPG) method (Atluri and Zhu, 1998), and the Corrective Smooth Particle Method (CSPM) (Chen, Beraun and Carney, 1999). The major difference among these methods lies in the interpolation techniques. The interested readers are referred to the work by Belytschko, Krongauz, Organ and Fleming (1996), Atluri and Shen (2002), and Liu (2002) for the similarities and differences among those meshless methods.

One unique advantage of the MLPG method is that no background mesh is used to evaluate various integrals appearing in the local weak formulation of problem. Therefore, the MLPG method is a "truly meshfree" approach in terms of both interpolation of variables and integration of energy. The latest development of the MLPG method can be found in Atluri (2005). It has been demonstrated to be quite successful in solving different branches of initial-boundary-value problems. In the application of the MLPG method to FGMs, Qian and Ching (2004) studied dynamic deformation of an FG beam and found that the maximum first frequency occurs in the FG beam rather than in the homogeneous beam. Qian and Batra (2004,2005) combined the MLPG method with a higher order plate theory to analyze the transient heat conduction and thermal stresses in a thick FG plate. Sladek J, Sladek V and Zhang (2003) and Sladek J, Sladek V, Krivacek and Zhang (2005) utilized local boundary integral equations to study elastodynamics and transient heat conduction in isotropic and anisotropic FG solids, respectively. Ching and Yen (2005) performed a steady-state thermomechanical analysis for 2-D FG solids in which the variation of material properties are either described by analytical functions or computed by micromechanical models.

Laser irradiation has been applied to examine the thermomechanical behavior of FGMs, specifically for the fracture process in a thermal barrier coating system (Takahasi, Ishikawa, Okugawa and Hashida, 1992). Elperin and Rudin (2002) developed an analytical procedure for solving transient 2-D temperature and thermal stress distribution in an FGM coating composed of tungsten carbide (WC) and steel, where the effective material properties were simply approximated by the "rule of mixture". In this paper, we employ the MLPG method to investigate the transient thermomechanical response of a two-phase metal/ceramic FG composite subjected to high-density laser heating. The spatially various effective thermoelastic properties are evaluated by the two different homogenization schemes. The paper is organized as follows: Section 2 gives governing equations for both thermoelastic and heat conduction analyses. In Section 3, the moving least squares (MLS) approximation, the weak formu-

lation of the MLPG method as well as the discrete system of equations are briefly presented. Two homogenization approaches for the effective material moduli, namely, the Mori-Tanaka method and the self-consistent method, are summarized in Section 4. Numerical results for a 2-D FG strip subjected to Gaussian laser beams are presented and discussed in Section 5. Conclusions are drawn in Section 6.

2 Governing Equations

For a 2-D isotropic solid occupying the domain Ω bounded by the boundary Γ and unstressed at a reference temperature, we use rectangular Cartesian coordinates $\mathbf{x} = \{x_1, x_2\}^T$ to describe its transient thermomechanical behaviors. The governing equations of the mechanical equilibrium in elastostatics with neglecting inertial and body forces and the transient thermal equilibrium in the absence of internal heat sources are given by

$$\sigma_{ij,j} = 0 \quad \text{in } \Omega \times [0,t] \tag{1}$$

$$-q_{j,j} = c\rho\dot{\theta} \quad \text{in } \Omega \times [0,t] \tag{2}$$

where σ_{ij}, q_j, c and ρ are the Cauchy stress tensor, the heat flux vector, the specific heat and the mass density, respectively; θ is the change in temperature with respect to the stress-free reference state. A comma followed by index j denotes partial differentiation with respect to coordinate x_j, a superimposed dot indicates partial derivative with respect to time t, and a repeated index implies summation over the range of the index. Equations (1) and (2) are supplemented with the following boundary conditions:

$$u_i = \overline{u}_i \quad \text{on } \Gamma_u \times [0,t] \tag{3a}$$

$$\sigma_{ij} n_j = \overline{t}_i \quad \text{on } \Gamma_t \times [0,t] \tag{3b}$$

and

$$\theta = \overline{\theta} \quad \text{on } \Gamma_\theta \times [0,t] \tag{4a}$$

$$q_j n_j = \overline{q} \quad \text{on } \Gamma_q \times [0,t] \tag{4b}$$

$$q_j n_j = h(\theta - \theta_s) \quad \text{on } \Gamma_h \times [0,t] \tag{4c}$$

where $\overline{u}_i$ are the prescribed displacements on Γ_u and $\overline{t}_i$ the given tractions on Γ_t with Γ_u and Γ_t being the complementary parts of the boundary Γ (i.e., $\Gamma_u \cap \Gamma_t = \phi, \Gamma_u \cup \Gamma_t = \Gamma$). The body is also subject to the thermal boundary conditions where the prescribed temperature $\overline{\theta}$ is specified on Γ_θ, the given heat flux $\overline{q}$ is imposed on Γ_q, and the convection heat loss to an ambient temperature θ_s occurs on Γ_h. Likewise, Γ_u, Γ_q and Γ_h constitute another set of complementary parts of the boundary. h is the coefficient of the convection, and n_j are the components of the unit outward normal to Γ. Since θ equals the temperature change, the initial condition is set to be $\theta(\mathbf{x}, 0) = 0$.

The constitutive equations for a linearly isotropic thermoelastic material are as follows:

$$\sigma_{ij} = \lambda\varepsilon_{kk}\delta_{ij} + 2\mu\varepsilon_{ij} - \beta\theta\delta_{ij} \tag{5}$$

$$q_j = -\kappa\theta_{,j} \tag{6}$$

where λ and μ are Lame'constants, β is the stress-temperature modulus, κ is the thermal conductivity, and ε_{ij} is the infinitesimal strain tensor which is related to the displacement field u_i by

$$\varepsilon_{ij} = \frac{1}{2}(u_{i,j} + u_{j,i}) \tag{7}$$

In this work, the interchange between thermal and mechanical energy is neglected since the laser heating considered is not ultrafast (Chen, Tham and Beraun, 2004). Thus, the uncoupled, quasi-static thermomechanical equations are solved in the sequence: the transient temperature field is first determined by solving Eqs. (2) and (6) and the relevant boundary and initial conditions, and then the displacements are computed from Eqs. (1), (5) and (7) with the predetermined temperature field and the pertinent boundary conditions.

3 The MLPG Formulation

3.1 Brief Description of the MLS Approximation

In the MLPG method, the moving least squares (MLS) approximation is adopted for forming the basis functions $\phi_i(\mathbf{x})$ for an unknown trial function; see Lancaster and Salkauskas (1981) for details. For completeness, we briefly describe below the MLS approximation. Let $f^h(\mathbf{x},t)$ be an approximation of a scalar function $f(\mathbf{x},t)$

$$f^h(\mathbf{x},t) = \mathbf{p}^T(\mathbf{x})\mathbf{a}(\mathbf{x},t) = \sum_{j=1}^{m} p_j(\mathbf{x}) a_j(\mathbf{x},t) \tag{8}$$

where $\mathbf{p}^T(x,y) = [p_1(\mathbf{x}), p_2(\mathbf{x}), ..., p_m(\mathbf{x})]$ is a vector of the complete monomial basis of order m. Examples of $\mathbf{p}^T(\mathbf{x})$ in a 2-D problem are:

$$\mathbf{p}^T(\mathbf{x}) = \{1, x_1, x_2\} \quad \text{for linear basis}, m = 3 \tag{9a}$$

$$\mathbf{p}^T(\mathbf{x}) = \left\{1, x_1, x_2, x_1^2, x_1x_2, x_2^2\right\} \quad \text{for quadratic basis}, m = 6 \tag{9b}$$

The m unknown coefficients $a_j(\mathbf{x},t)$ are determined by minimizing a weighted discrete L_2 norm defined by

$$J = \sum_{i=1}^{n} W(\mathbf{x}-\mathbf{x}_i)[\mathbf{p}^T(\mathbf{x}_i)\mathbf{a}(\mathbf{x},t) - \hat{f}_i(t)]^2 \tag{10}$$

where n is the number of points in the neighborhood of point $\mathbf{x}$ for which the weight functions $W(\mathbf{x}-\mathbf{x}_i) > 0$, and $\hat{f}_i(t)$ refers to the nodal variable at time t of the function $f$at point $\mathbf{x}_i$. We choose the following Gaussian distribution to be the weight function:

$$W(\mathbf{x}-\mathbf{x}_i) = \begin{cases} \frac{\exp[-(d_i/c_i)^{2k}]-\exp[-(r_i/c_i)^{2k}]}{1-\exp[-(r_i/c_i)^{2k}]} & 0 \le d_i \le r_i \\ 0 \quad d_i \ge r_i \end{cases} \tag{11}$$

where $d_i = |\mathbf{x}-\mathbf{x}_i|$ is the distance between points $\mathbf{x}$ and $\mathbf{x}_i$, c_i is the distance from node i to its third nearest neighboring node, and r_i is the radius of the circle outside of which $W(\mathbf{x}-\mathbf{x}_i)$ vanishes.

Finding the extremum of J in Eq. (10) with respect to $\mathbf{a}(\mathbf{x},t)$ leads to the following system of linear equations for the determination of $\mathbf{a}(\mathbf{x},t)$:

$$\mathbf{A}(\mathbf{x})\mathbf{a}(\mathbf{x},t) = \mathbf{B}(\mathbf{x})\hat{\mathbf{f}} \tag{12}$$

where

$$\mathbf{A}(\mathbf{x}) = \sum_{i=1}^{n} W(\mathbf{x}-\mathbf{x}_i)\mathbf{p}(\mathbf{x}_i)\mathbf{p}^T(\mathbf{x}_i) \tag{13a}$$

$$\mathbf{B}(\mathbf{x} = [W(\mathbf{x}-\mathbf{x}_1)\mathbf{p}(\mathbf{x}_1), W(\mathbf{x}-\mathbf{x}_2)\mathbf{p}(\mathbf{x}_2), ..., W(\mathbf{x}-\mathbf{x}_n)\mathbf{p}(\mathbf{x}_n)] \tag{13b}$$

Solving $\mathbf{a}(\mathbf{x},t)$ from Eq. (12) and substituting it into Eq. (8), we have the following relation for the nodal interpolation

$$f^h(\mathbf{x},t) = \sum_{i=1}^{n} \phi_i(\mathbf{x})\hat{f}_i(t) \tag{14}$$

with

$$\phi_i(\mathbf{x} = \sum_{j=1}^{m} p_j(\mathbf{x})[\mathbf{A}^{-1}(\mathbf{x})\mathbf{B}(\mathbf{x})]_{ji} \tag{15}$$

$\phi_i(\mathrm{x})$is usually called the basis function of the MLS approximation corresponding to node i. Note that $\phi_i(\mathbf{x}_j)$ need not equal the Kronecker delta δ_{ij}, and thus $\hat{f}_i(t) \neq f^h(\mathbf{x}_i,t)$. For the matrix $\mathbf{A}$ to be invertible, the number of n points must at least equal m (e.g. $n \ge m$). For m = 3 or 6, Chati and Mukherjee (2004) suggest that $15 \le n \le 30$ give acceptable results for 2-D elastostatic problems. In this study, we choose m = 6 and k = 1 in Eq. (11) and take

$$r_i = 4c_i \tag{16}$$

3.2 Weak Formulation and Discretization

In this section, a weak or variational formulation corresponding to the governing equations (1) and (2) and the boundary conditions (3) and (4) is presented. The system equations are obtained by discretizing the weak formulation using the moving least squares method. We first give the weak formulation and its discrete form for the thermoelastic analysis, and the equations for the transient heat conduction analysis then can be obtained in a similar manner.

3.2.1 Thermoelastic analysis

Let $\xi(\mathbf{x}) = \{\xi_1, \xi_2\}^T$be a set of test functions where ξ_1 and ξ_2 are two linearly independent functions defined in Ω. Taking the inner product of Eq. (1) with ξ and of Eq. (3a) with $\chi\xi$, integrating the resulting equations over Ω and Γ_u, respectively, and adding them, utilizing the integration by parts as well as the divergence theorem, and imposing the natural boundary condition (3b) on Γ_t, we obtain

$$\int_\Omega \tilde{\varepsilon}^T \sigma d\Omega - \int_{\Gamma_u} \xi^T \mathbf{N}\sigma d\Gamma - \int_{\Gamma_t} \xi^T \bar{\mathbf{t}} d\Gamma + \chi \int_{\Gamma_u} \xi^T(\mathbf{u}-\bar{\mathbf{u}})d\Gamma = 0 \tag{17}$$

where $\chi >> 1$ is a penalty parameter. The penalty method is chosen here for imposing essential boundary condition (3a) due to the lack of the Kronecker delta property of the basis function $\phi_i(\mathbf{x})$. It has been shown that the penalty method performs with higher efficiency

than the method of the Lagrange multipliers (e.g. see Belytschko, Lu and Gu, 1994) and the orthogonal transformation technique (e.g. see Atluri, Kim and Cho, 1999). However, the selection of the penalty parameter still remains a challenge as the parameter cannot be taken 'very large' in order to avoid ill-conditioned of the system matrix. A suitable range for the value of the penalty parameter suggested by Zhu and Atluri (1998) is $\chi = (10^3 \sim 10^7) \cdot E$, where E is Young's modulus of the material.

The constitutive equation for thermal stresses is written in the matrix form

$$\sigma = \{\sigma_{11},\ \sigma_{22}, \sigma_{12}\}^T = \mathbf{D}\varepsilon - \beta\theta \tag{18}$$

where $\mathbf{D}$ is the matrix of elastic constants and β the matrix of the stress-temperature moduli; both may be functions of $\mathbf{x}$. For a two-dimensional isotropic solid, $\mathbf{D}$ becomes

$$D = \frac{\overline{E}(\mathbf{x})}{1-\overline{\nu}(\mathbf{x})^2}\begin{bmatrix} 1 & \overline{\nu}(\mathbf{x}) & 0 \\ \overline{\nu}(\mathbf{x}) & 1 & 0 \\ 0 & 0 & (1-\overline{\nu}(\mathbf{x})/2 \end{bmatrix} \tag{19}$$

$$\overline{E} = \begin{cases} E & \\ \frac{E}{1-\nu^2} & \end{cases} \qquad \overline{\nu} = \begin{cases} \nu & \text{for plane stress} \\ \frac{\nu}{1-\nu} & \text{for plane strain} \end{cases} \tag{20}$$

and β is given by

$$\beta = \beta(\mathbf{x}) \begin{Bmatrix} 1 \\ 1 \\ 0 \end{Bmatrix} \tag{21}$$

$$\beta = \frac{\alpha E}{1-\nu} \text{ (plane stress)}, \ \beta = \frac{\alpha E}{1-2\nu} \text{ (plane strain)} \tag{22}$$

The strain $\tilde{\varepsilon}$ in Eq. (17) can be obtained from the following equation by replacing displacement components u_i with the test functions ξ_i

$$\varepsilon = \begin{Bmatrix} \varepsilon_{11} \\ \varepsilon_{22} \\ \gamma_{12} \end{Bmatrix} = \begin{Bmatrix} \frac{\partial u_1(\mathbf{x})}{\partial x_1} \\ \frac{\partial u_2(\mathbf{x})}{\partial x_2} \\ \frac{\partial u_2(\mathbf{x})}{\partial x_1} + \frac{\partial u_1(\mathbf{x})}{\partial x_2} \end{Bmatrix} \tag{23}$$

The matrix $\mathbf{N}$ in Eq. (17) is

$$\mathbf{N} = \begin{bmatrix} n_1 & 0 & n_2 \\ 0 & n_2 & n_1 \end{bmatrix} \tag{24}$$

The most distinguished feature of the MLPG method is that the weak formulation is based on a local sub-domain rather than a global problem domain. We assume that N nodes are placed in Ω and S_1, S_2,... S_N are smooth 2-D closed regions, not necessarily disjoint and of the same shape and size. Let $\phi_1, \phi_2, ...\phi$ and $\psi_1,\ \psi_2, ... \psi_n$ be two sets of linearly independent functions defined over a region, say S_α. The unknown trial function $\mathbf{u}$ and the test function ξ can be written respectively by

$$\mathbf{u}(\mathbf{x}) = \begin{Bmatrix} u_1(\mathbf{x}) \\ u_2(\mathbf{x}) \end{Bmatrix} = \sum_{J=1}^{n} \mathbf{\Phi}_J(\mathbf{x})\widehat{\mathbf{u}}_J \tag{25}$$

$$\xi(\mathbf{x}) = \begin{Bmatrix} \xi_1(\mathbf{x}) \\ \xi_2(\mathbf{x}) \end{Bmatrix} = \sum_{I=1}^{n} \mathbf{\Psi}_I(\mathbf{x})\widehat{\xi}_I \tag{26}$$

where $\mathbf{\Phi}_J = \phi_J\mathbf{I}$ and $\mathbf{\Psi}_I = \psi_I\mathbf{I}$; $\mathbf{I}$ is a 2×2 identity matrix; $\widehat{\mathbf{u}}_J$ and $\widehat{\xi}_I$ are 2×1 arrays. Various options of the test function leading to different MLPG formulations have been discussed by Atluri and Shen (2002). Here, we equal the test function to the weight function of the moving least squares approximation. Substitution of Eqs. (25) and (26) into (23) for ε and $\tilde{\varepsilon}$, respectively, results in

$$\varepsilon = \sum_{J=1}^{n} \mathbf{B}_J\widehat{\mathbf{u}}_J \quad \tilde{\varepsilon} = \sum_{I=1}^{n} \tilde{\mathbf{B}}_I\widehat{\xi}_I \tag{27}$$

where

$$\mathbf{B}_J = \begin{bmatrix} \frac{\partial\phi_J}{\partial x_1} & 0 \\ 0 & \frac{\partial\phi_J}{\partial x_2} \\ \frac{\partial\phi_J}{\partial x_2} & \frac{\partial\phi_J}{\partial x_1} \end{bmatrix} \quad \tilde{\mathbf{B}}_I = \begin{bmatrix} \frac{\partial\psi_I}{\partial x_1} & 0 \\ 0 & \frac{\partial\psi_I}{\partial x_2} \\ \frac{\partial\psi_I}{\partial x_2} & \frac{\partial\psi_I}{\partial x_1} \end{bmatrix} \tag{28}$$

Replacing the domain Ω of integration in Eq. (17) by S_α, substituting for $\mathbf{u}$, $\tilde{\mathbf{u}}$, ε, and $\tilde{\varepsilon}$ from Eqs. (25) and (26), and requiring that the resulting equations hold for all choices of $\widehat{\xi}_I$, we arrive at the following linear alge-

braic equations for $\widehat{\mathbf{u}}_J$:

$$\sum_{J=1}^{n}\int_{S_\alpha}\tilde{\mathbf{B}}_I^T\mathbf{D}\mathbf{B}_J\widehat{\mathbf{u}}_J d\Omega-\sum_{J=1}^{n}\int_{\Gamma_{\alpha u}}\mathbf{\Psi}_I^T\mathbf{S}\mathbf{N}\mathbf{D}\mathbf{B}_J\widehat{\mathbf{u}}_J d\Gamma + \sum_{J=1}^{n}\chi\int_{\Gamma_{\alpha u}}\mathbf{\Psi}_I^T\mathbf{S}\mathbf{\Phi}_J\widehat{\mathbf{u}}_J d\Gamma = \int_{S_\alpha}\tilde{\mathbf{B}}_I^T\beta\theta d\Omega-\int_{\Gamma_{\alpha u}}\mathbf{\Psi}_I^T\mathbf{S}\mathbf{N}\beta\theta d\Omega + \int_{\Gamma_{\alpha t}}\mathbf{\Psi}_I^T\overline{\mathbf{t}}d\Gamma+\chi\int_{\Gamma_{\alpha u}}\mathbf{\Psi}_I^T\overline{\mathbf{u}}d\Gamma \quad (I=1,2,\ldots,n) \tag{29}$$

where

$$\mathbf{S}=\begin{bmatrix} S_1 & 0\\ 0 & S_2\end{bmatrix}$$

$$S_i=\begin{cases} 1 & \text{if } u_i \text{ is prescribed on } \Gamma_u\\ 0 & \text{if } u_i \text{ is not prescribed on } \Gamma_u\end{cases} \tag{30}$$

Symbolically, the simultaneous equations (29) are written as

$$\mathbf{K}_\alpha\widehat{\mathbf{u}}_\alpha=\mathbf{F}_\alpha \tag{31}$$

The final system of equations can be obtained by repeating Eq. (28) for each of all the N nodes.

The weak formulation can also be obtained from the variational form for linear elastic analysis by using the so-called Duhamel-Neumann principle (Sokolnikoff, 1956) in which the body force $\mathbf{b}$ is replaced by $\mathbf{b}-\beta\nabla\theta$ and the prescribed tractions $\overline{\mathbf{t}}$ on Γ_t replaced by $\overline{\mathbf{t}}+\theta\beta\mathbf{n}$. For example, Bobaru and Mukherjee (2002) utilized this principle and gave the weak formulation of the Element Free Galerkin method for thermoelastic analysis.

3.2.2 Transient heat conduction analysis

Let $\eta(\mathbf{x})$ be another test function defined over Ω. Following the procedure in the above thermoelastic analysis, the weak formulation associated with the governing equation (2) and the boundary conditions (4) can be written as

$$\int_\Omega\nabla^T\eta\mathbf{q}d\Omega-\int_\Omega\eta c\rho\dot{\theta}d\Omega-\int_{\Gamma_\theta}\eta\mathbf{n}^T\mathbf{q}d\Gamma - \int_{\Gamma_q}\eta\overline{q}d\Gamma-\int_{\Gamma_h}\eta h(\theta-\theta_s)d\Gamma +\chi\int_{\Gamma_\theta}\eta(\theta-\overline{\theta})d\Gamma=0 \tag{32}$$

Here, $\mathbf{q}$ is the vector of heat flux and is related to the Fourier heat conduction law by

$$\mathbf{q}=\{q_1,q_2\}^T=-\kappa\nabla\theta \tag{33}$$

with

$$\nabla\theta=\begin{Bmatrix}\theta_{,1}\\ \theta_{,2}\end{Bmatrix}=\begin{Bmatrix}\frac{\partial\theta(\mathbf{x})}{\partial x_1}\\ \frac{\partial\theta(\mathbf{x})}{\partial x_2}\end{Bmatrix} \tag{34}$$

The unknown trial function θ and the test function η can also be expressed in an interpolative form as

$$\theta(\mathbf{x})=\sum_{J=1}^{n}\phi_J(\mathbf{x})\widehat{\theta}_J \tag{35a}$$

$$\eta(\mathbf{x})=\sum_{I=1}^{n}\psi_I(\mathbf{x})\widehat{\eta}_I \tag{35b}$$

Substitution of Eqs. (35a) and (35b) into (34) gives

$$\nabla\theta=\sum_{J=1}^{n}\mathbf{C}_J\widehat{\theta}_J \tag{36a}$$

$$\nabla\eta=\sum_{I=1}^{n}\tilde{\mathbf{C}}_I\widehat{\eta}_I \tag{36b}$$

with

$$\mathbf{C}_J=\begin{bmatrix}\frac{\partial\phi_J}{\partial x_1}\\ \frac{\partial\phi_J}{\partial x_2}\end{bmatrix} \tag{37a}$$

$$\tilde{\mathbf{C}}_I=\begin{bmatrix}\frac{\partial\psi_I}{\partial x_1}\\ \frac{\partial\psi_I}{\partial x_2}\end{bmatrix} \tag{37b}$$

Substituting for θ, η, $\nabla\theta$, $\nabla\eta$ from Eqs. (35) and (36) into (32) for the region S_α and requiring that the resulting equations hold for all choices of $\widehat{\eta}_I$, we arrive at the following system equation:

$$\sum_{J=1}^{n}\mathbf{M}_{IJ}\dot{\widehat{\theta}}_J+\mathbf{L}_{IJ}\widehat{\theta}_J=\sum_{J=1}^{n}\mathbf{G}_I\quad(I=1,2,...,n) \tag{38}$$

where

$$\mathbf{M}_{IJ}=\int_{S_\alpha}c\rho\psi_I\phi_J\mathrm{d}\Omega \tag{39a}$$

$$\mathbf{L}_{IJ} = \int_{S_\alpha} \tilde{\mathbf{C}}_I^T \kappa \mathbf{C}_J d\Omega - \int_{\Gamma_{\alpha\theta}} \psi_I \kappa \mathbf{n}^T \mathbf{C}_J d\Gamma + \int_{\Gamma_{\alpha h}} h\psi_I \phi_J d\Gamma - \chi \int_{\Gamma_{\alpha\theta}} \psi_I \phi_J d\Gamma \tag{39b}$$

$$\mathbf{G}_I = -\int_{\Gamma_{\alpha q}} \psi_I \overline{q} d\Gamma - \chi \int_{\Gamma_{\alpha\theta}} \psi_I \overline{\theta} d\Gamma + \int_{\Gamma_{\alpha h}} h\psi_I \theta_S d\Gamma \tag{39c}$$

Repeating Eq. (38) for the nodes in the entire domain leads to the system of equations.

A numerical integration is required to evaluate the domain integral on S_α and the line integral on ∂S_α in Eqs. (28) and (38). The region S_α, and the boundary $\Gamma_{\alpha u}, \Gamma_{\alpha t}, \Gamma_{\alpha q}, \Gamma_{\alpha\theta}$ and $\Gamma_{\alpha h}$ on ∂S_α are mapped onto a $[-1, 1] \times [-1, 1]$ square domain and a $[-1, 1]$ straight line, respectively, and the Gauss quadrature rule is utilized to numerically evaluate these integrals. Therefore, no shadow cells are needed for the purpose of integration.

We use the generalized trapezoidal rule (Cook, Malkus and Plesha, 1989) to integrate Eq. (38). The recursive relation for temperature between the time interval Δt is

$$\overset{\sim}{\theta}_J^{t+\Delta t} = \overset{\sim}{\theta}_J^{t} + \Delta t \left\{ (1-\beta) \overset{\cdot}{\overset{\sim}{\theta}}_J^{t} + \beta \overset{\cdot}{\overset{\sim}{\theta}}_J^{t+\Delta t} \right\} \tag{40}$$

where $\overset{\sim}{\theta}_J^{t}$ and $\overset{\cdot}{\overset{\sim}{\theta}}_J^{t}$ denote the temperature, the time derivative of temperature, respectively, at time t, and β is a parameter that controls the stability and the accuracy of the time integration scheme. The algorithm is unconditionally stable if

$$\beta \geq \frac{1}{2} \tag{41}$$

Depending on the value of β, different time integration schemes can be obtained. In this study, the popular choice of $\beta = 1/2$, which is known as the Crank-Nicolson method, is employed.

4 Estimation of Effective Moduli

Analytical functions such as the exponent and power law functions are commonly used in describing the continuously varying material properties in FGMs because these functions facilitate obtaining exact solutions for the analysis of FGM structures. However, this approach may not describe the physical variation of material properties in most FGMs. Another approximation for the effective material properties of FGMs is the rule of mixtures. Again, this method does not account for the interaction between phases, and thus it only gives very approximate values for most of the effective moduli. A more theoretically sound approach is the micromechanical models, among which the Hashin-Shtrikman bounds (Hashin and Shtrikman, 1963), the Mori-Tanaka method (Mori and Tanaka, 1973), the self-consistent method (Hill, 1965), and the mean field approach (Wakashima and Tsukamoto, 1991) are the popular ones. The micromechanical approach takes account of the interactions and uses a certain representative volume element (RVE) to solve the average local stress and strain fields of the constituents of the composite. In the present study, the effective heat capacity (ρc) is estimated by the "rule of mixture". For the effective Young's modulus, Poisson's ratio, thermal conductivity, and the coefficient of thermal expansion, we implement two homogenization schemes, the Mori-Tanaka method and the self-consistent method, to compute the properties. For brevity, these two methods are summarized below.

4.1 Mori-Tanaka Method

The Mori-Tanaka method assumes that the matrix phase, denoted by the subscript 1, is reinforced by spherical particles of a particulate phase, denoted by the subscript 2. In this notation, K_1, μ_1, κ_1, α_1 represent the bulk modulus, shear modulus, thermal conductivity and coefficient of thermal expansion, respectively, V_1 the volume fraction of the matrix phase, and K_2, μ_2, κ_2, α_2 and V_2 the corresponding material properties and the volume fraction of the particulate phase.

For a two-phase composite, the effective bulk modulus K and shear modulus μ derived by Mori-Tanaka (1973) are given as

$$\frac{K-K_1}{K_2-K_1} = \frac{V_2}{1+(1-V_2)(K_2-K_1)/(K_1+4\mu_1/3)} \tag{42}$$

$$\frac{\mu-\mu_1}{\mu_2-\mu_1} = \frac{V_2}{1+(1-V_2)(\mu_2-\mu_1)/(\mu_1+f_1)} \tag{43}$$

where $f_1 = \mu_1(9K_1+8\mu_1)/6(K_1+2\mu_1)$, and $V_1+V_2=1$. The Young's modulus and Poisson's ratio are related to the bulk and shear moduli by $E = 9K\mu/(3K+\mu)$ and $\nu = (3K-2\mu)/2(3K+\mu)$, respectively.

The effective thermal conductivity κ derived by Hatta

and Taya (1985) is

$$\frac{\kappa-\kappa_1}{\kappa_2-\kappa_1}=\frac{V_2}{1+(1-V_2)(\kappa_2-\kappa_1)/3\kappa_1} \tag{44}$$

and the coefficient of thermal expansion α derived by Rosen and Hashin (1970) is

$$\frac{\alpha-\alpha_1}{\alpha_2-\alpha_1}=\frac{1/K-1/K_1}{1/K_2-1/K_1} \tag{45}$$

4.2 *Self-consistent method*

The self-consistent method assumes that each reinforcement inclusion is embedded in a continuum material whose effective properties are those of the composite. This method does not distinguish between matrix and reinforcement phases, and the same overall moduli are predicted in another composite in which the roles of the phases are interchanged. This makes it particularly suitable for determining the effective moduli in those regions that have an inter-connected skeletal microstructure.

For a two-phase composite, the effective bulk modulus K and shear modulus μ are obtained by solving the following coupled equations (Hill, 1965):

$$\frac{1}{K+4\mu/3}=\frac{V_1}{K_1+4\mu/3}+\frac{V_2}{K_2+4\mu/3} \tag{46}$$

$$\frac{V_1K_1}{K_1+4\mu/3}+\frac{V_2K_2}{K_2+4\mu/3}+5\left(\frac{V_1\mu_2}{\mu-\mu_2}+\frac{V_2\mu_1}{\mu-\mu_1}\right)+2=0 \tag{47}$$

The self-consistent model of the thermal conductivity coefficient κ derived by Hashin (1968) is in the implicit form as

$$\frac{V_1(\kappa_1-\kappa)}{\kappa_1+2\kappa}+\frac{V_2(\kappa_2-\kappa)}{\kappa_2+2\kappa}=0 \tag{48}$$

Equation (45) is used to evaluate the coefficient of thermal expansion α with K_1, K_2, α_1, α_2 and the effective bulk modulus Kdetermined form Eqs. (46) and (47).

Figure 1 shows the effective properties as functions of the volume fraction of V_2 computed with the two homogenization schemes. It can be seen that the Mori-Tanaka method results in larger values for the effective Poisson's ratio, coefficient of thermal expansion, and thermal conductivity but smaller values for the effective Young's modulus.

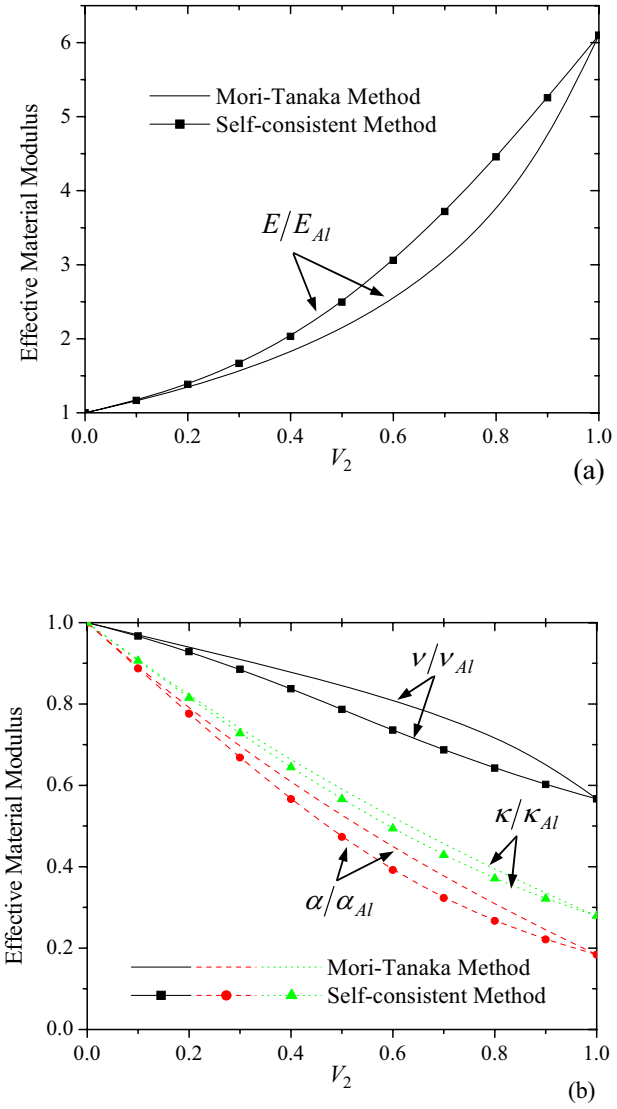

Figure 1 : Variations of the effective material moduli computed by the Mori-Tanaka method and self-consistent method with the volume fraction of V_2; (a) Young's modulus, (b) Poisson's ratio, (c) coefficient of thermal expansion, and (d) thermal conductivity

5 Results and Discussion

A computer code based on the aforestated MLPG formulation was developed and used to analyze transient thermoelastic response of 2-D FG solids composing of *Al* metal and *SiC* ceramic phases. Figure 2 depicts a schematic sketch of the problem studied. The FG strip with L = 50 *mm* and H = 10 *mm* (i.e. length-to-thickness ratio: $L/H=5$) is irradiated by a Gaussian laser beam.

Table 1 : Material properties for *Al* and *SiC*

Property	*Al*	*SiC*
Young's modulus E (GPa)	70	427
Poisson's ratio ν	0.3	0.17
Coefficient of thermal expansion α $(/K)$	23.4×10^{-6}	4.3×10^{-6}
Thermal conductivity κ (W/mK)	233	65
Specific Heat c (J/KgK)	896	670
Density ρ (Kg/m^3)	2707	3100

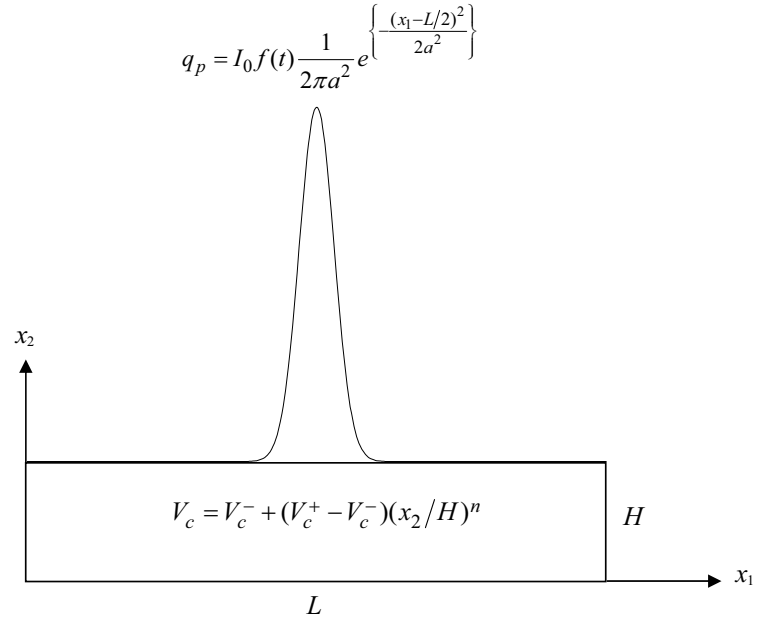

Figure 2 : An FG composite subjected to the Gaussian laser heat flux on the top surface

The intensity distribution q_p of the absorbed laser energy is expressed as

$$q_p = I_o f(t) \frac{1}{2\pi a^2} e^{-\frac{(x_1 - L/2)^2}{2a^2}} \tag{49}$$

where I_0 is the laser beam power, a is the beam radius, and the temporal function is assumed to be $f(t) = (1 - e^{-\gamma t})$ with γ being a time rise constant. The bottom surface is thermally insulated (i.e. q = 0), and the two edges of the strip are simply-supported and held at a reference temperature at all times

$$\begin{aligned} &u_2(0, x_2, t) = u_2(L, x_2, t) = 0; \\ &\theta(0, x_2, t) = \theta(L, x_2, t) = 0 \end{aligned} \tag{50}$$

Material properties of *Al* and *SiC* are listed in Table 1. The volume fraction of the ceramic phase varies over the thickness by a power law function

$$V_c = V_c^- + (V_c^+ - V_c^-)(x_2/H)^n \tag{51}$$

where V_c^+ and V_c^- are the volume fractions of *SiC* on the top and the bottom surfaces, respectively; n is a power law index that dictates the volume fraction profile through the thickness. Effective material properties of the 2-D FG strips are evaluated by both the Mori-Tanaka method and the self-consistent method with the ceramic *SiC* taken as phase 2. The through-the-thickness effective properties are plotted in Fig. 3 for different values of n, computed with the two sets of micromechanical models respectively.

Due to symmetry of the problem about the vertically centroidal plane, only one half of the domain is analyzed under the plane stress state. Unless otherwise specified,

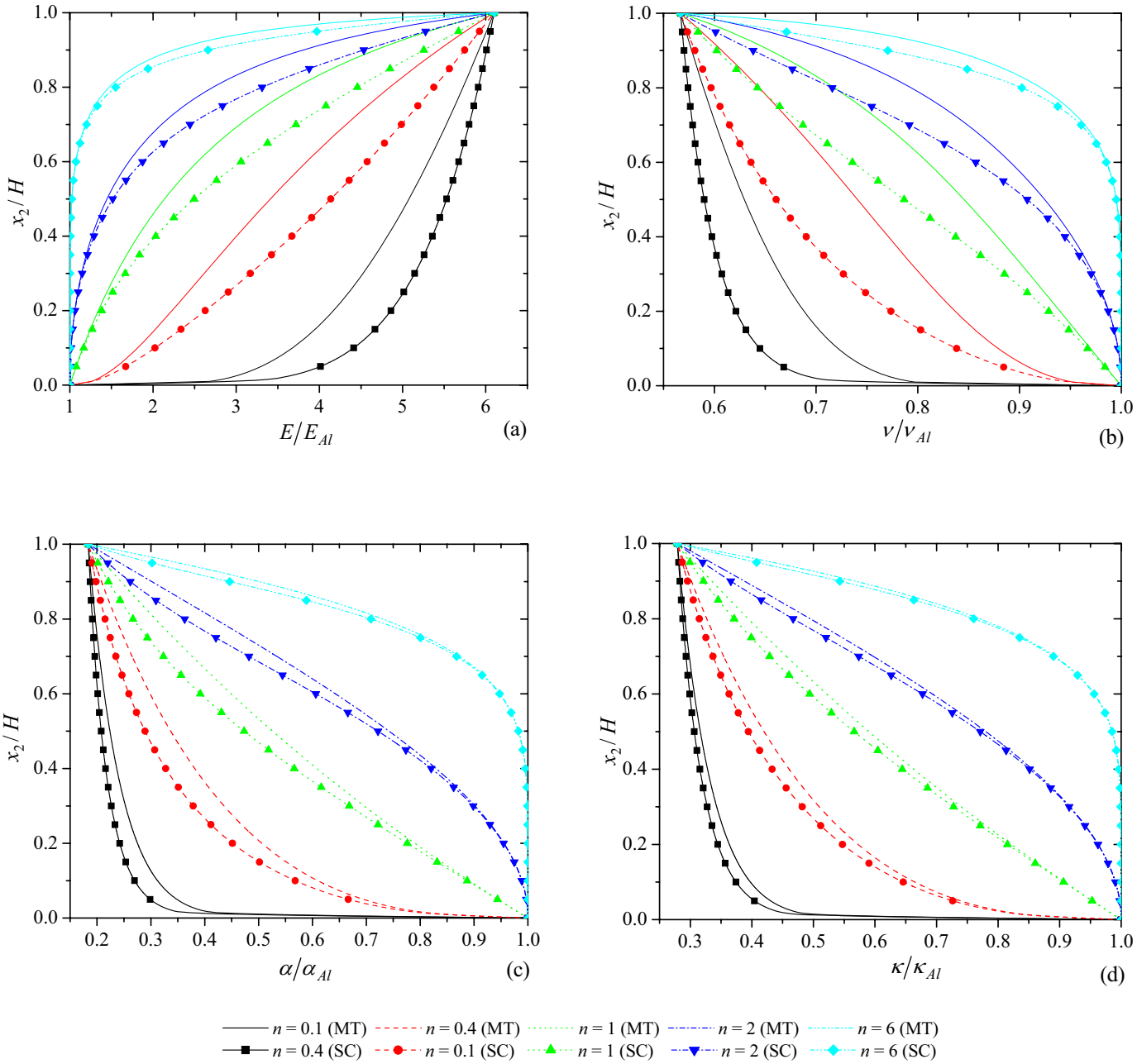

Figure 3 : Through-the-thickness variations of the effective material moduli obtained by the Mori-Tanaka method and self-consistent method for different values of the power law index n; (a) Young's modulus, (b) shear modulus, (c) coefficient of thermal expansion, and (d) thermal conductivity

typical values are given for V_c^+= 1.0, V_c^- = 0, n = 2,γ = 10.0 s^{-1}, I_0 = 400 W, $a = a_0$= 1 mm, and the Mori-Tanaka method is a default homogenization scheme in the analyses. Numerical results are presented in terms of the nondimensional variables defined by

$$\left[\overline{\theta},\ \overline{u}_2,\ \overline{\sigma}_{11},\ \overline{\sigma}_{12}\right] = \frac{2\pi a_0^2}{I_0}\left[\frac{\kappa_{Al}\theta}{H},\ \frac{10\kappa_{Al}u_2}{\alpha_{Al}L^2},\ \frac{100\kappa_{Al}\sigma_{11}}{E_{Al}\alpha_{Al}L},\ \frac{1000\kappa_{Al}\sigma_{12}}{E_{Al}\alpha_{Al}L}\right] \tag{52}$$

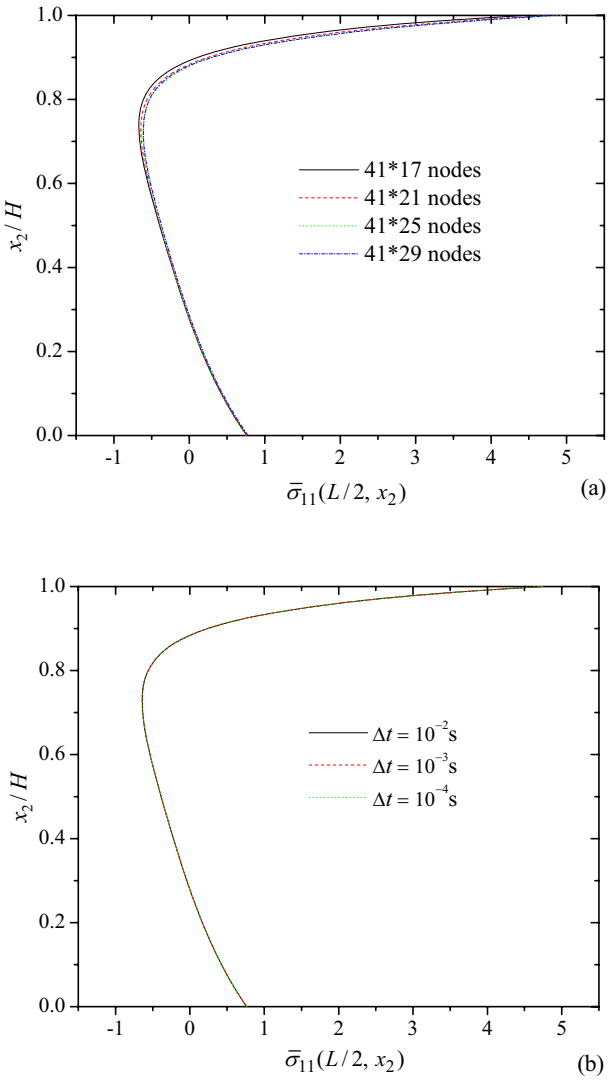

Figure 4 : Through-the-thickness variations of the normalized longitudinal stress along the vertically centroidal surface at t= 2s for (a) four different nodal densities and (b) three different time steps; results are computed by the Mori-Tanaka method for the *Al/SiC* FG strip under the high heat flux of the laser heating on the top surface with $\gamma = 10.0\text{s}^{-1}$, $V_c^- = 0$, $V_c^+ = 1$ and $n = 2$

The convergence study for the nodal density and time step is first examined. Figure 4(a) compares the variation of the longitudinal stress $\overline{\sigma}_{11}$ through the vertically centroidal surface of the FG strip for the four different nodal densities at t = 2 s. In theses calculations we fix 41 equally spaced nodes along the x_1 direction and use 17, 21, 25 and 29 nodes along the x_2 direction. Results in Fig. 4(a) reveal that the simulated longitudinal stresses are almost identical for the four sets of nodal density, thus indicating that the convergence regarding the spatial discretization has been achieved. For the time step size, three different time steps $\Delta t = 10^{-2}$ s, 10^{-3} s and 10^{-4} s are chosen. It is found from Fig. 4(b) that the variations of the longitudinal stress are also indistinguishable. This means that a time step of $\Delta t = 10^{-2}$s already gives essentially converged results. Therefore, we use a nodal mesh of 49×25 nodes and the time step size of 10^{-3}s in the following calculations.

Figures 5(a-d) show the time histories of temperature $\overline{\theta}$,transverse displacement $\overline{u}_2$, longitudinal stress $\overline{\sigma}_{11}$, and transverse shear stress $\overline{\sigma}_{12}$ at different points in the FG strip for $\gamma = 10.0\ \text{s}^{-1}$, $1.0\ \text{s}^{-1}$, and $0.1\ \text{s}^{-1}$. It appears that for $\gamma = 10.0\ \text{s}^{-1}$, all of the physical quantities reach the steady state rapidly while the change is more gradual for $\gamma = 0.1\ \text{s}^{-1}$. The steady state is reached at about $t = 20$ s for $\gamma = 10.0\ \text{s}^{-1}$, $t = 25$ s for $\gamma = 1.0\ \text{s}^{-1}$, and $t = 50$ s for $\gamma = 0.1\ \text{s}^{-1}$. Regardless of the values of γ, the temperature at the centroid and the longitudinal stress at the center of top surface increase monotonically to their steady state values, while this is not always the case for the transverse displacement and the transverse shear stress. For example, the transverse displacement moves upward (i.e. in the positive x_2 direction) in the early time, but then deflects downward and increases in magnitude until the steady sate establishes.

Through-the-thickness variations of the temperature, transverse displacement and longitudinal stress at $x_1 = L/2$, and the transverse shear stress at $x_1 = 0$ are plotted in Figs. 6(a-d) for time t = 0.5 s, 5 s and 50 s. Clearly, the temperature increases monotonically with its maximum values always occurring on the top (heated) surface. In general, the Mori-Tanaka micromechanical approach computes lower temperature than the self-consistent approach, especially in the region near the irradiated surface. This is because more heat diffuses away due to the larger effective thermal conductivity described by the Mori-Tanaka method (Fig 3(a)). In the early times (e.g. t = 0.5 s), the transverse displacement calculated with the Mori-Tanaka approach is positive but changes to negative as time increases. The change is mainly caused by bending due to the different thermal expansion ($\alpha\Delta\overline{\theta}$) in the upper (hotter) and lower (colder) regions. From Figs. 3(c) and 6(a), the ratio of $\alpha\Delta\overline{\theta}$ at the top and bottom surfaces is found to be about 3.0 at t = 0.5 s, 1.3 at t = 1.0

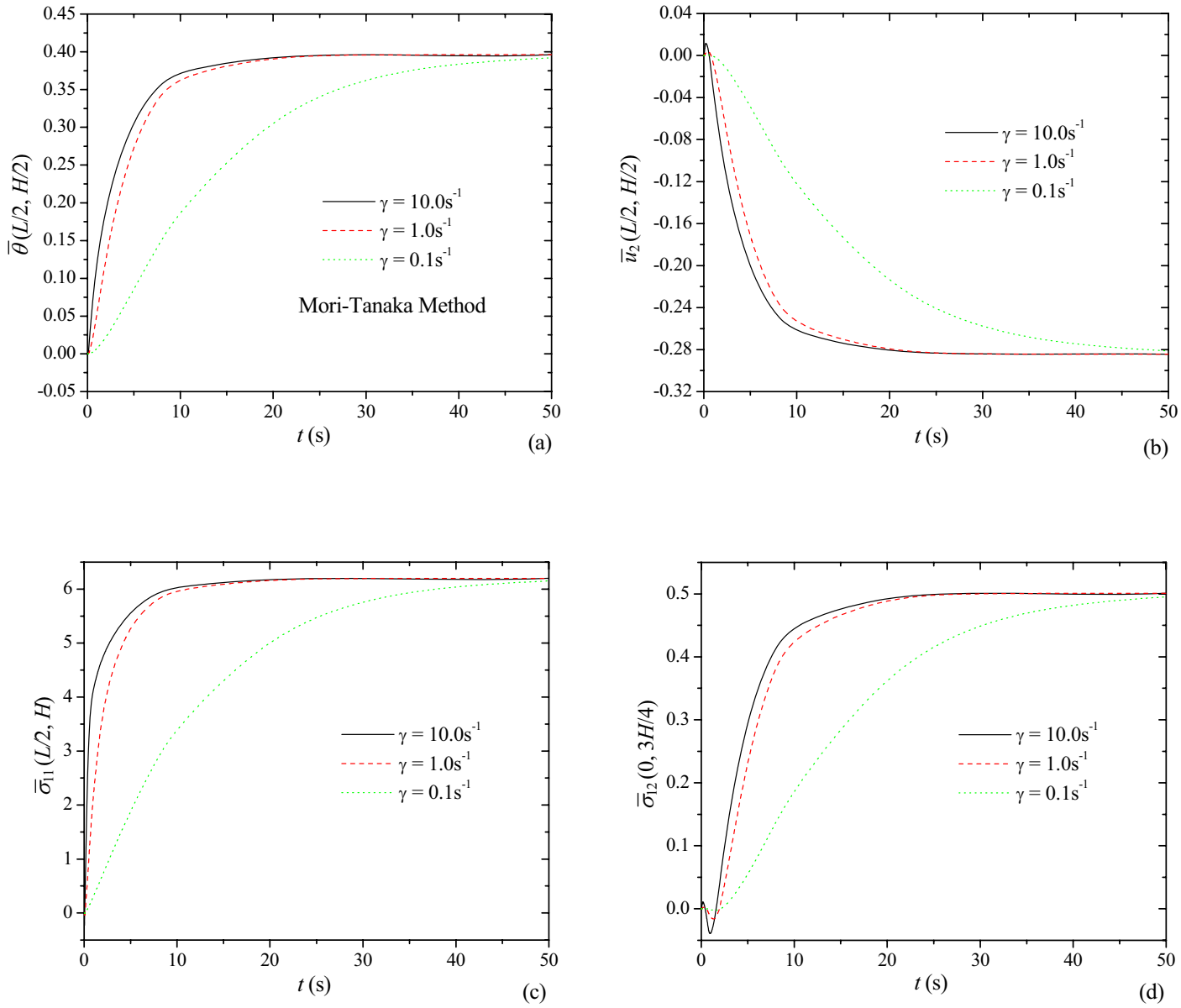

Figure 5 : Time histories of the normalized (a) temperature change, (b) transverse displacement, (c) longitudinal stress and (d) transverse shear stress, computed by the Mori-Tanaka method for different values of γ with $V_c^- = 0, V_c^+ = 1$ and $n = 2$

s, and 0.44 at t = 50 s. A greater expansion in the top portion would deflect the media upward, and thereby resulting in the positive transverse displacement. This occurs during the early times. An opposite conclusion can be made for the late times, as the greater thermal expansion occurring in the lower portion evidenced by the ratio of $\alpha\Delta\overline{\theta}$ at the two surfaces becomes 0.44 at t = 50 s. The less pronounced bending effect found for the Mori-Tanaka method in Fig. 6(b) is due to the larger difference of the effective thermal expansion coefficient in the top region between the two methods. At these three time instants, the calculated longitudinal stress is in tension near the top and bottom surfaces and in compression in the middle region of the FG strip. The transverse shear stress consists of two half-sine waves of different amplitudes through the thickness.

Figures 7(a-d) show the dependences of the temperature,

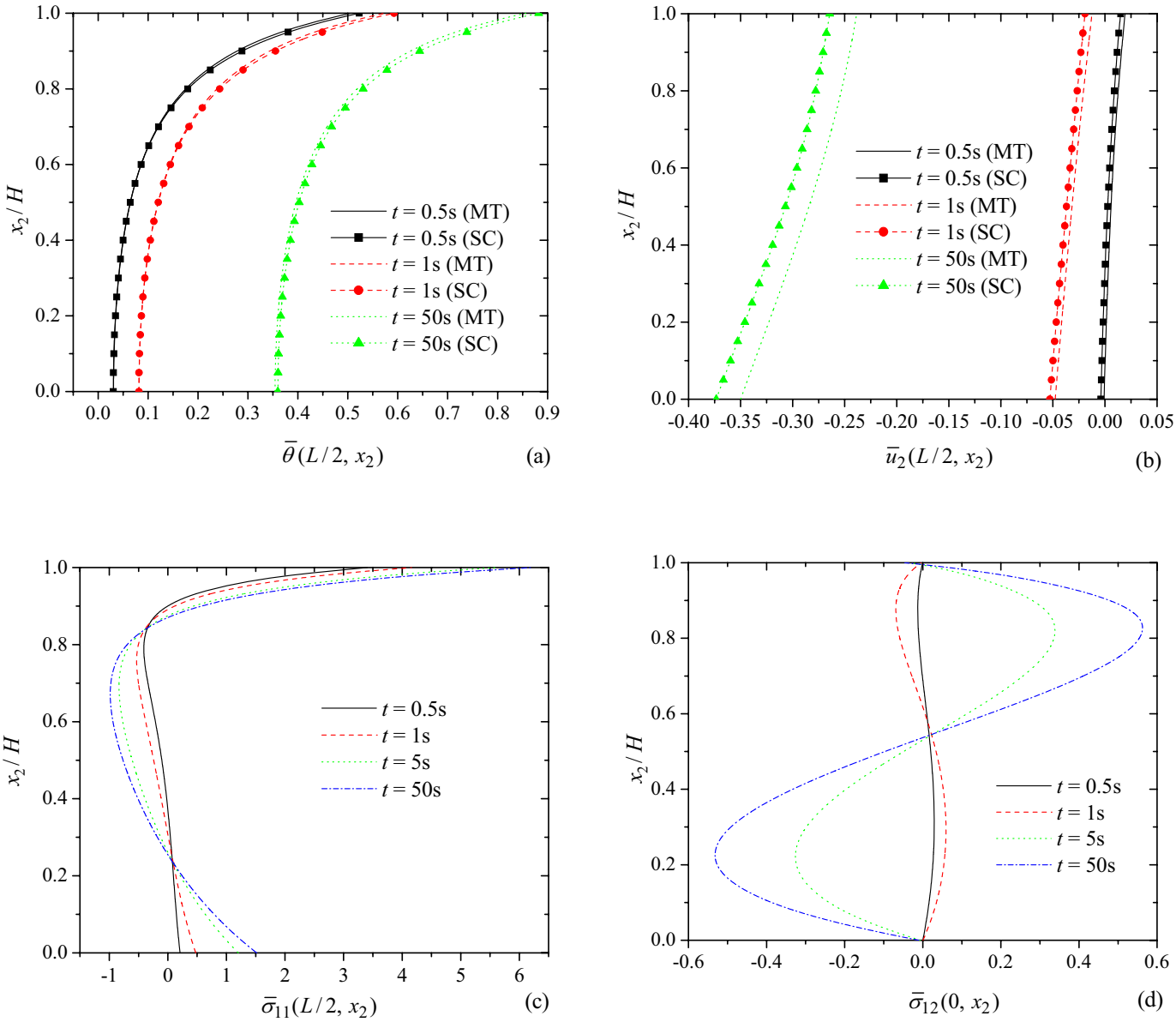

Figure 6 : Through-the-thickness variations of the normalized (a) temperature change and (b) transverse displacement computed by the Mori-Tanaka method and self-consistent method at t = 0.5s, 1s and 50s, and (c) longitudinal stress and (d) transverse shear stress computed by the Mori-Tanaka method at t = 0.5s, 1s , 5s and 50s; $V_c^- = 0, \quad V_c^+ = 1, \gamma = 10.0\text{s}^{-1}$ and $n = 2$

transverse displacement, longitudinal stress and transverse stress on the power law index n, computed by the Mori-Tanaka method and the self-consistent method. Although the temperature obtained from the two micromechanical approaches are quite close in both the transient and steady states, the other physical quantities agree qualitatively but differ quantitatively. As shown in Fig. 7(a), the temperature at the centroid of the FG strip decreases as n increases, and is always lower than that in a pure ceramic strip (i.e. n = 0). This is because the heat capacity (ρc) of *SiC* is smaller than that of *Al*. The lower temperature predicted by the Mori-Tanaka approach than that by the self-consistent approach is due to the larger effective thermal conductivity predicted by the former, as explained previously. The trend of monotonic decrease with n for temperature does not apply to the transverse

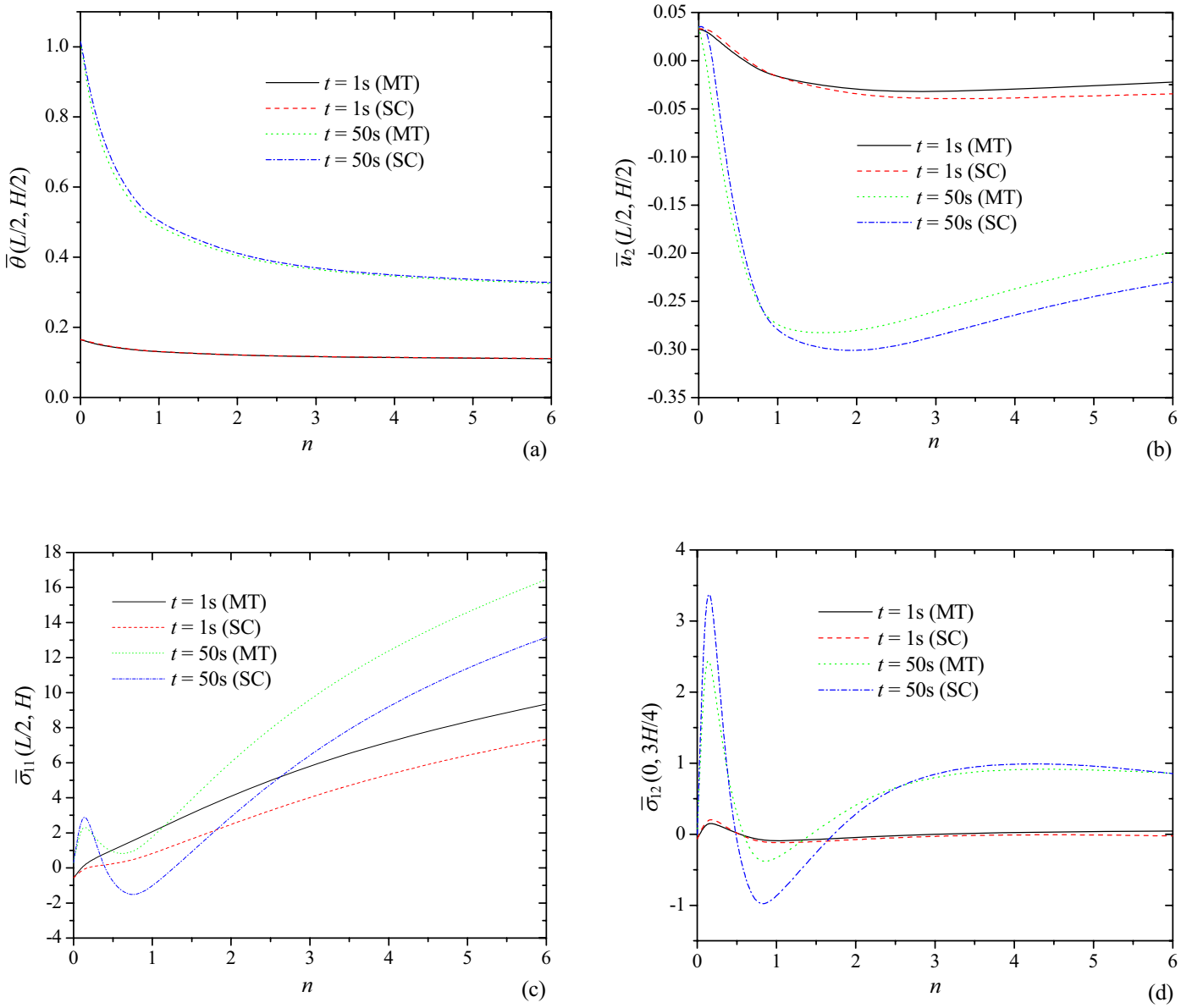

Figure 7 : Variations of the normalized (a) temperature change, (b) transverse displacement, (c) longitudinal stress, and (d) transverse shear stress with the power law index n, computed by both the Mori-Tanaka method and self-consistent method with $\gamma = 10.0\text{s}^{-1}$, $V_c^- = 0$, and $V_c^+ = 1$ at t = 1s and 50s

displacement. Instead, Fig. 7(b) shows the magnitude of the transverse displacement is in positive first and decreases with n, reaches the maximum negative value, and then increases. This behavior, again, can be explained by the different thermal expansion between the upper and lower regions. When the power index n becomes large enough, the displacement sign will change back to positive as that seen for small n. The non-monotonic change with n is also seen for the stresses in Figs. 7(c) and 7(d).

Figures 8(a) and 8(b) display the time histories of the temperature and transverse displacement at the centroid of the strip for four different values of n. Again, the temperature and deformation in the FGMs differ substantially from those of their homogeneous counterpart (n = 0).

With the significant discrepancy of the thermomechanical results obtained by the Mori-Tanaka method and the

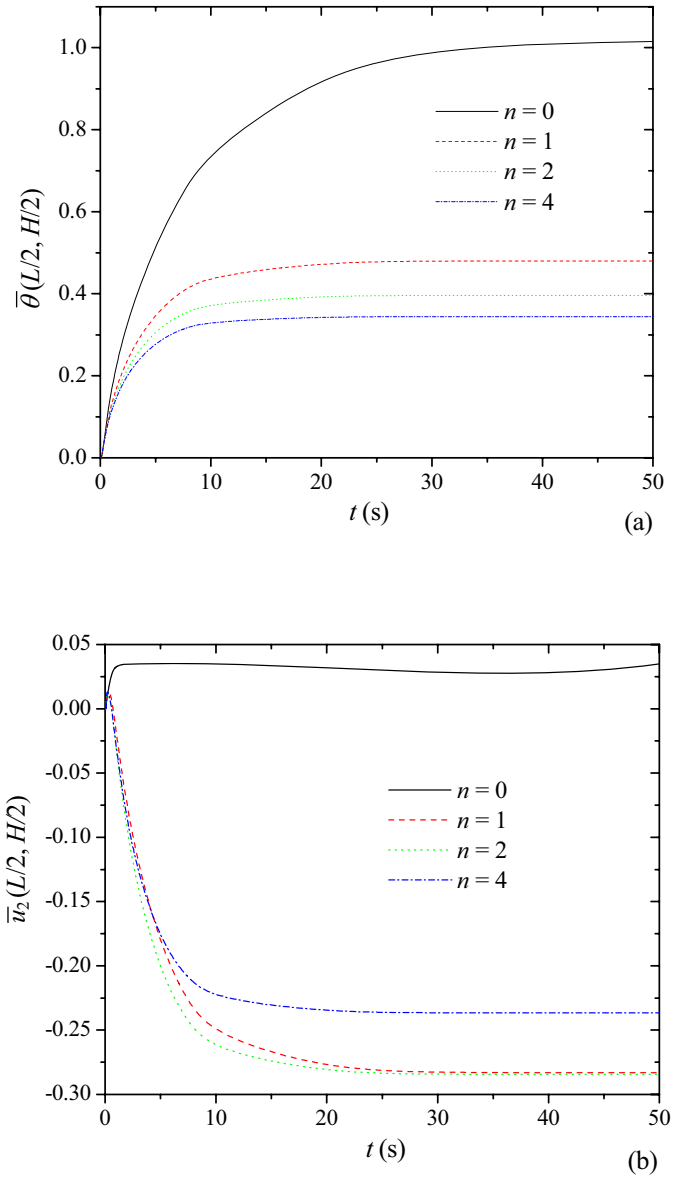

Figure 8 : Time histories of the normalized (a) temperature change and (b) transverse displacement computed by the Mori-Tanaka method for different values of the power law index n with $\gamma = 10.0\text{s}^{-1}$, $V_c^- = 0$, and $V_c^+ = 1$

self-consistent method found in Figs. 7(b-d), it is worth noting here that a high fidelity micromechanical model of the effective properties is important in the investigation of FGMs.

Figures 9(a) and 9(b) delineate the variations of the transverse displacement and longitudinal stress with the value V_c^+ when n is fixed to 2. Unlike the influence of the index n in those quantities (c.f. Figs. 7(b) and 7(c)), the transverse displacement and the longitudinal stress are monotonic functions of V_c^+. At both t = 1 s and 50 s, the magnitude of the transverse displacement increases with the increase of V_c^+. The trend also holds for the longitudinal stress. The corresponding time evolutions for different values of V_c^+ are shown in Figs. 9(c) and 9(d), respectively.

In Figs. 10(a) and 10(b), we compare through-the-thickness variations of the transverse shear stress along the left edge for different V_c^+ at the early time (t = 1 s) and the steady state, respectively. At the steady state, the magnitude of the shear stress at a point increases as V_c^+ increases. In a transient state, however, the magnitude does not necessarily increases with the increase in V_c^+. When $V_c^+ = 0$, the FG strip is recovered to a pure aluminum strip. As seen in Fig. 10(b), no shear stress is induced in the pure aluminum strip at the steady state.

Figures 11(a) and 11(b) show the effects of the laser beam radius on the temperature and the longitudinal stress induced along the vertically centroid surface, respectively. It is evident that under the same laser power, a smaller laser beam results in greater temperature rise, thereby causing more severe thermal stresses. At t = 1 s, the temperature at the center of the irradiated surface rises up to $4107\,^\circ K(\overline{\theta} = 1.503)$, $1567\,^\circ K(\overline{\theta} = 0.574)$, $874\,^\circ K(\overline{\theta} = 0.320)$, and $569\,^\circ K(\overline{\theta} = 0.208)$ for the beam radius of a = 0.5 *mm*, 1.0 *mm*, 1.5 *mm* and 2.0 *mm,* respectively. Hence, for typical values of the parameters studied here (i.e. a = 1 *mm* and I_o = 400 *W*), one can heat the surface of the FG strip at a rate of $1000\,^\circ K/s$, which is usually required for the thermal reliability of specimens. Under this operating condition, the induced tensile stress is found to be 0.93 *GPa* ($\overline{\sigma}_{11} = 4.160$). Elperin and Rudin (2002) also showed that the temperature of an FGM coating under the laser heating increases as the laser beam radius decreases. In their study, a similar heating rate of $1000\,^\circ K/s$by a laser beam of power 1 *KW* and radius 1 $\sim$ 2 *mm* is reported.

6 Conclusions

We have presented the MLPG analysis for thermoelastic response of a 2-D *Al/SiC* functionallity graded composite subjected to high intensity laser irradiation. The effective material properties are evaluated from the local volume fraction of ceramic and metal phases by using two homogenization schemes. It is shown that a tai-

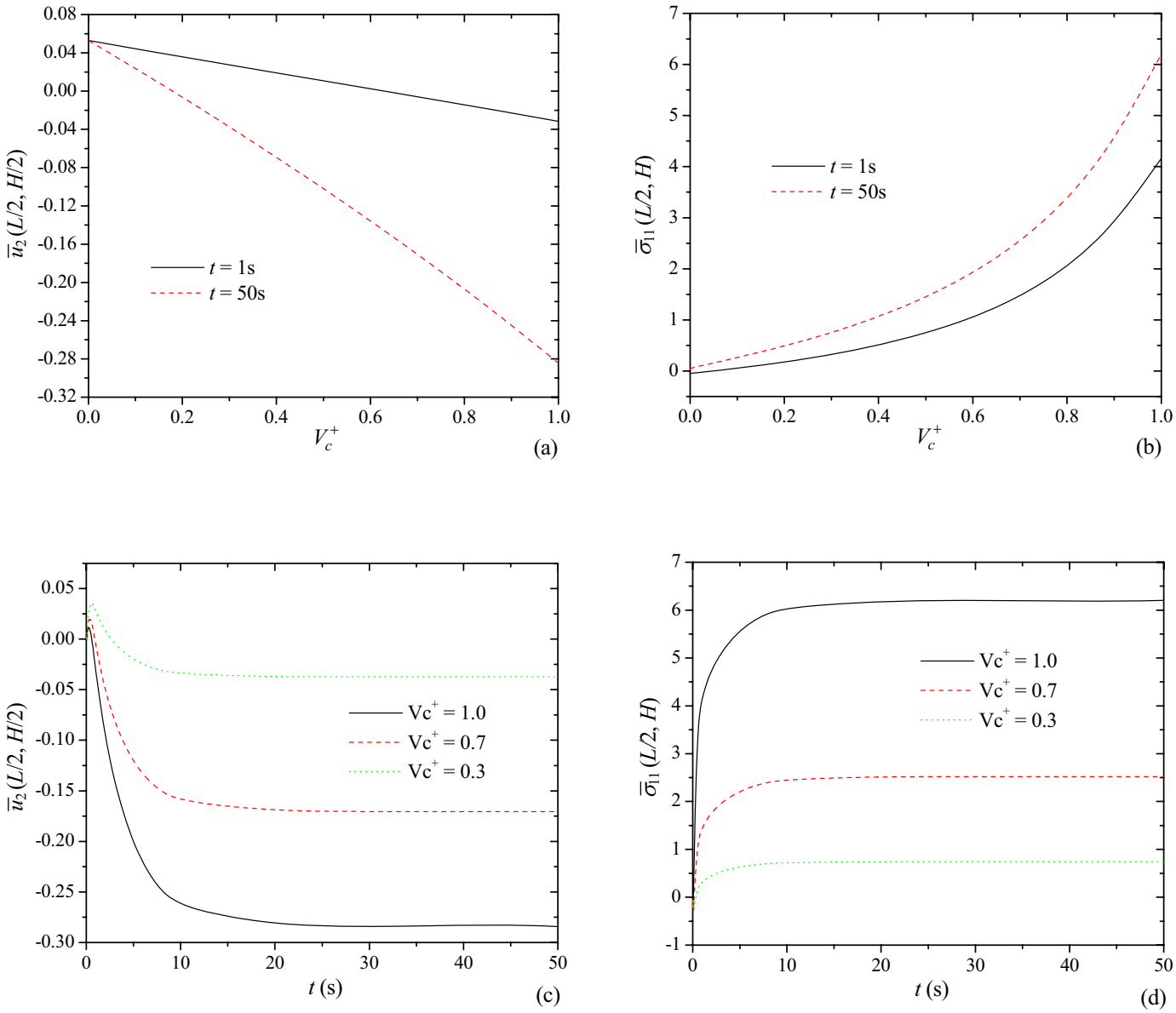

Figure 9 : Variations of the normalized (a) transverse displacement and (b) longitudinal stress with volume fraction V_c^+; the time histories of the normalized (c) transverse displacement and (d) longitudinal stress for different values of V_c^+; results are computed by the Mori-Tanaka method for $\gamma = 10.0\text{s}^{-1}$, $V_c^- = 0$, and $n = 2$

lored FGC can significantly alter the temperature and deformation fields as compared to those for their homogeneous counterparts. An increase of the power law index n in the material composition distribution $V_c = V_c^- + (V_C^+ - V_c^-)(x_2/H)^n$ can result in a decrease of the temperature change, but the trend is not always true for the stresses. For a fixed power index n, both the displacement and stresses induced change monotonically with the increase of V_C^+, the ceramic volume fraction on the top surface. It is also found that the thermomechanical results obtained with the effective properties of FGCs computed by the Mori-Tanaka method and the self-consistent method are significantly different. Therefore, it is important to use a high fidelity model of the effective properties in the investigation of FGCs. In addition, lasers of the same power that has a smaller beam size not only results in greater temperature but also causes higher stress in the FG strip studied.

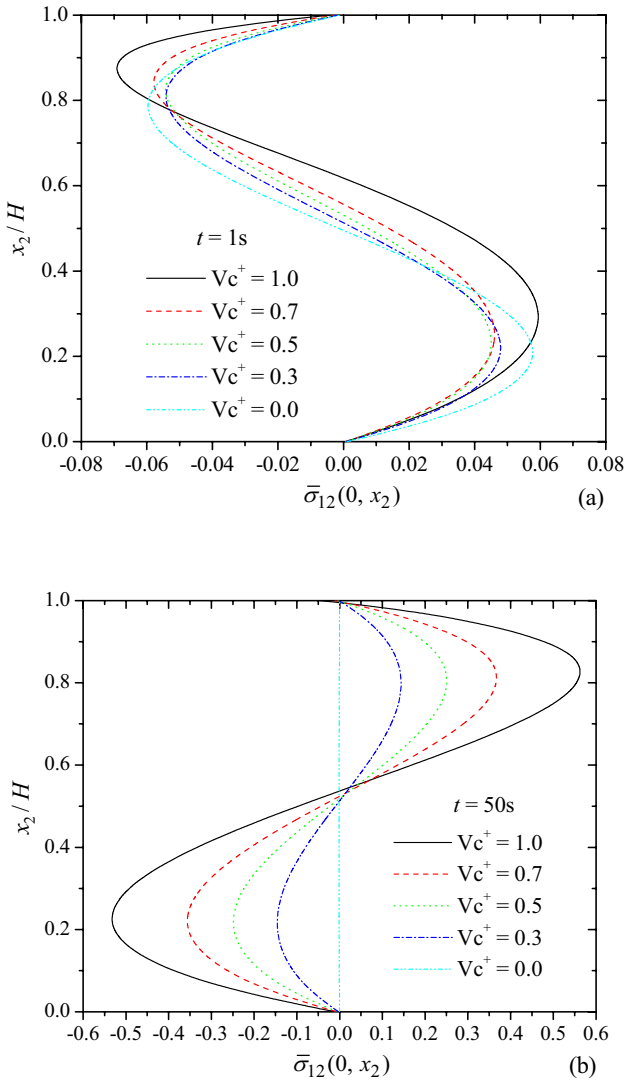

Figure 10 : Through-the-thickness variations of the normalized transverse shear stress computed by the Mori-Tanaka method for different values of volume fraction V_c^+ at (a) t = 1s and (b) t = 50s with γ = 10.0s^{-1}, $V_c^- = 0$, and $n = 2$

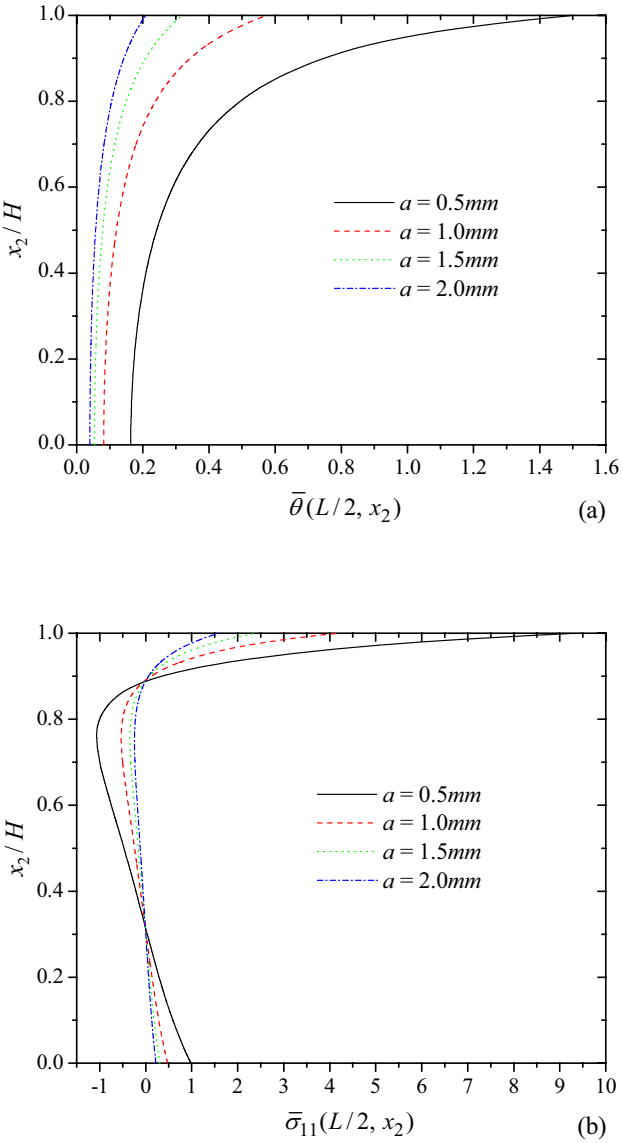

Figure 11 : Through-the-thickness variations of the normalized (a) temperature change and (b) longitudinal stress computed by the Mori-Tanaka method for different values of a at t = 1s with γ = 10.0s^{-1}, $V_c^- = 0$, $V_c^+ = 1$ and $n = 2$

Unlike finite element methods, the MLPG method requires only a set of nodes for both the interpolation of the trial functions and the integration of the weak forms. Moreover, this meshfree method dictates the continuous material properties of FGMs directly to a quadrature point. These prominent features make the MLPG method well-suited in the analysis of functionally graded composite structures.

References

Atluri S.N. (2005): The Meshless Method (MLPG) for Domain and BIE Discretizations. Los Angeles, USA: Tech. Science Press.

Atluri S.N.; Kim H.G.; Cho J.Y. (1999): A Critical Assessment of the Truly Meshless Local Petrov-Galerkin (MLPG) and Local Boundary Integral Equation (LBIE)

Methods. *Computational Mechanics*, vol. 24(5), pp. 348-372.

Atluri S.N.; Shen S.P. (2002): The Meshless Local Petrov-Galerkin (MLPG) Method. Los Angeles, USA: Tech. Science Press.

Atluri S.N.; Zhu T. (1998): A New Meshless Local Petrov-Galerkin (MLPG) Approach in Computational Mechanics. *Computational Mechanics*, vol. 22, pp. 117-127.

Awaji H.; Sivakumar R. (2001): Temperature and Stress Distributions in a Hollow Cylinder of Functionally Graded Material: The Case of Temperature-Independent Material Properties. *Journal of American Ceramic Society*, vol. 85(5), pp. 1059-1065.

Belytschko T., Krongauz Y., Organ D.J., Fleming M., Krysl P. (1996): Meshless Methods: an Overview and Recent Developments. *Computer Methods in Applied Mechanics and Engineering*, vol. 139, pp. 3-47.

Belytschko T.; Lu Y.Y.; Gu L. (1994): Element-free Galerkin methods. *International Journal for Numerical Methods in Engineering*, vol. 37, pp. 229-256.

Bobaru F.; Mukherje S. (2002): Meshless Approach to Shape Optimization of Linear Thermoelastic Solids. *International Journal for Numerical Methods in Engineering*, vol. 53, pp. 765-796.

Chati M.K.; Mukherjee S. (2000): The Boundary Node Method for Three-Dimensional Problems in Potential Theory. *International Journal for Numerical Methods in Engineering*, vol. 47, pp. 1523-1547.

Chen J.K.; Beraun J.E.; Carney T.C. (1999): A Corrective Smoothed Particle Method for Boundary Value Problems in Heat Conduction. *International Journal for Numerical Methods in Engineering*, vol. 46 (2), pp. 231-252.

Chen J.K.; Tham C.L.; Beraun J.E. (2004): Ultrafast Thermoelasticity for Short-Pulse Laser Heating. *International Journal of Engineering Science*, vol. 42 (8-9). pp. 793-807.

Ching H.K.; Yen S.C. (2005): Meshless Local Petrov-Galerkin Analysis for 2-D Functionally Graded Elastic Solids under Mechanical and Thermal Loads. *Composites Part B*: *Engineering,* vol. 33, pp. 223-240.

Cook R.D.; Malkus D.S.; Plesha M.E. (1989): Concepts and Applications of Finite Element Analysis. 3th Edition: John Wiley & Sons, Inc.

Duarte C.A.; Oden J.T. (1996): H-*p* clouds ? an *hp* Meshless Method. *Numerical Methods for Partial Differential Equations*, vol. 12, pp. 673-705.

Elperin T.; Rudin G. (2002): Thermal Stresses in Functionally Graded Materials Caused by a Laser Thermal Shock. *Heat and Mass Transfer*, vol. 38, pp. 625-630.

Hashin Z. (1968): Assessment of the Self-Consistent Scheme Approximation: Conductivity of Particulate Composites. Journal of Composite Materials 1968; 2: 284-300.

Hashin Z.; Shtrikman S. (1963): A Variational Approach to the Theory of Elastic Behavior of Multiphase Materials. *Journal of the Mechanics and Physics of Solids*, vol. 11(2), pp 127-140.

Hatta H.; Taya M. (1985): Effective Thermal Conductivity of a Misoriented Short Fiber Composite. *Journal of Applied Physics*, vol. 58, pp. 2478-2486.

Hill R. (1965): A Self-Consistent Mechanics of Composite Materials. *Journal of the Mechanics and Physics of Solids*, vol. 13(2), pp. 213-222.

Jin Z.H.; Paulino G.H. (2001): Transient Thermal Stress Analysis of an Edge Crack in a Functionally Graded Material. *International Journal of Fracture*, vol. 107(1), pp. 73-98.

Lancaster P.; Salkauskas K. (1981): Surfaces Generated by Moving Least Squares Methods. *Math. Comput.*, vol. 37, pp. 141-158.

Liu G.R. (2002): Mesh Free Method: Moving Beyond the Finite Element Method. CRC Press.

Liu W.K.; Jun S.; Zhang Y.F. (1995): Reproducing Kernel Particle Methods. *International Journal for Numerical Methods in Engineering*, vol. 20, pp. 1081-1106.

Melenk J.M.; Babuska I. (1996): The Partition of Unity Finite Element Method: Basic Theory and Applications. *Computer Methods in Applied Mechanics and Engineering*, vol. 139, pp. 289-314.

Mori T.; Tanaka K. (1973): Average Stress in Matrix and Average Elastic Energy of Materials with Misfitting Inclusions. *Acta Metallurgica*, vol. 21, pp. 571-574.

Nayroles B.; Touzot G.; Villon P. (1992): Generalizing the Finite Element Method: Diffuse Approximation and Diffuse Elements. *Computational Mechanics*, vol. 10, pp. 307-318.

Noda N. (1999): Thermal Stresses in Functionally Graded Materials. *Journal of Thermal Stresses*, vol.

22(4-5), pp. 477-512.

Ootao Y,; Tanigawa Y. (2004): Transient Thermooelastic Problem of Functionally Graded Thick Strip due to Nonuniform Heat Supply. *Composite Structures*, vol. 63, pp. 139-146.

Ootao Y,; Tanigawa Y. (2005): Three-dimensional Solution for Transient Thermal Stresses of Functionally Graded Rectangular Plate due to Nonuniform Heat Supply. *International Journal of Mechanical Sciences*, vol. 47(11), pp. 1769-1788.

Praveen G.N.; Chin C.D.; Reddy J.N. (1999): Thermoelastic Analyses of Functionally Graded Ceramic-Metal Cylinder. *Journal of Engineering Mechanics*, vol. November, pp. 1259-1267.

Qian L.F.; Batra R.C. (2004): Transient Thermoelastic Deformations of a Thick Functionally Graded Plate, *Journal of Thermal Stresses*, vol. 27, pp. 705-740.

Qian L.F.; Batra R.C. (2005): Three-Dimensional Transient Heat Conduction in a Functionally Graded Thick Plate with a Higher-Order Plate Theory and a Meshless Local Petrov-Galerkin Method, *Computational Mechanics*, vol. 35, pp. 214-226.

Qian L.F.; Ching H.K. (2004): Static and Dynamic Analysis of 2-D Functionally Graded Elasticity by Using Meshless Local Petrov-Galerkon Method. *Journal of the Chinese Institute of Engineers*, vol. 27, pp. 491-503.

Rosen B.W.; Hashin Z. (1970): Effective Thermal Expansion Coefficients and Specific Heats of Composite Materials. *International Journal of Engineering Science*, vol. 8, pp. 157-173.

Sladek J.; Sladek V.; Krivacek J.; Zhang C. (2005): Meshless local Petrov-Galerkin Method for Stress and Crack Analysis in 3-D Axisymmetric FGM Bodies. *CMES: Computer Modeling in Engineering & Sciences*, vol. 8 (3), vol. 259-270.

Sladek J.; Sladek V.; Zhang C. (2003): Application of Meshless Local Petrov-Galerkin (MLPG) Method to Elastodynamic Problems in Continuously Nonhomogeneous Solids. *CMES: Computer Modeling in Engineering & Sciences*, vol. 4(6), pp. 637-647.

Sokolnikoff I.S. (1956): Mathematical Theory of Elasticity. 2nd Edition: McGraw Hill.

Takahashi H.; Ishikawa T.; Okugawa D.; Hashida T. (1992): Laser and Plasma-arc Thermal Shock Fatigue Fracture Evaluation Procedure for Functionally Graded Materials. In: NATO ASI Series E: Appl. Sci., *Thermal Shock and Thermal Fatigue Behavior of Advance Ceramics*, vol. 241, pp. 543-554.

Ueda S. (2001): Thermoelastic Analysis of W-Cu Functionally Graded Materials Subjected to a Thermal Shock using a Micromechanical Model. *Journal of Thermal Stresses*, vol. 24(1), pp 19-46.

Vel S.S.; Batra R.C. (2003): Three-Dimensional Analysis of Transient Thermal Stresses in Functionally Graded Plates. *International Journal of Solids and Structures*, vol. 40, pp. 7181-7196.

Wakashima K.; Tsukamoto H. (1991): Mean-Field Micromechanics Model and its Application to the Analysis of Thermomechanical Behavior of Composite Materials. *Materials Science and Engineering A*, vol. 146, pp. 291-316.

Wang B.L.; Mai Y.W. (2005): Transient One-dimensional Heat Conduction Problems Solved by Finite Element. *International Journal of Mechanical Sciences*, vol. 47, pp. 303-317.

Wang B.L.; Tian Z.H. (2005): Application of Finite Element – Finite Difference Method to the Determination of Transient Temperature Field in Functionally Graded Materials. *Finite Elements in Analysis and Design*, vol. 41, pp. 335-349.

Zhu T.; Atluri S.N. (1998): A Modified Collocation Method and a Penalty Formulation for Enforcing the Essential Boundary Conditions in the Element Free Galerkin Method. *Computational Mechanics*, vol. 21, pp. 211-222.